




# Versatile application of a modern scanning electron microscope for materials characterization

Cheng Sun<sup>1,\*</sup> , Stefan Lux<sup>1</sup>, Erich Müller<sup>1</sup>, Matthias Meffert<sup>1</sup>, and Dagmar Gerthsen<sup>1</sup>

<sup>1</sup> *Karlsruher Institut Fur Technologie, Karlsruhe, Germany*

**Received:** 5 May 2020

**Accepted:** 13 June 2020

**Published online:**

6 July 2020

© The Author(s) 2020

## ABSTRACT

Scanning electron microscopy (SEM) is an indispensable characterization technique for materials science. More recently, scanning electron microscopes can be equipped with scanning transmission electron microscopy (STEM) detectors, which considerably extend their capabilities. It is demonstrated in this work that the correlative application of SEM and STEM imaging techniques provides comprehensive sample information on nanomaterials. This is highlighted by the use of a modern scanning electron microscope, which is equipped with in-lens and in-column detectors, a double-tilt holder for electron transparent specimens and a CCD camera for the acquisition of on-axis diffraction patterns. Using multi-walled carbon nanotubes and Pt/Al<sub>2</sub>O<sub>3</sub> powder samples we will show that a complete characterization can be achieved by combining STEM (mass-thickness and diffraction) contrast and SEM (topography and materials) contrast. This is not possible in a standard transmission electron microscope where topography information cannot be routinely obtained. We also exploit the large tilt angle range of the specimen holder to perform 180 degrees STEM tomography on multi-walled carbon nanotubes, which avoids the missing wedge artifacts.

## Introduction

Scanning electron microscopy (SEM) has become an indispensable tool in material research ever since its invention. Due to the possibility of high-resolution surface topography imaging of bulk samples and comparable low cost of scanning electron microscopes, SEM is one of the most important microscopy techniques and is available in many laboratories.

Recent advances in resolution and the implementation of scanning (S) TEM detectors in scanning electron microscopes extend the capability of these instruments by allowing the study of electron-transparent specimens [1–3]. Considering that STEM in scanning electron microscopes is performed at electron energies  $\leq 30$  keV, it is often referred to as low-keV STEM, STEM-in-SEM or transmission (T) SEM [4]. Compared to STEM in transmission electron microscopes operated at electron energies  $\geq 80$  keV, STEM-in-SEM is advantageous for the study of

Address correspondence to E-mail: cheng.sun@kit.edu

weakly scattering objects and materials sensitive to knock-on damage [5]. For example, STEM-in-SEM was demonstrated to be well suited for polymer analysis [6, 7]. With the enhanced contrast, it is possible to differentiate materials with similar material density and mean atomic number, which is often difficult by TEM [8]. Also, the wider field-of-view offers advantages, especially when imaging biomaterials with large volume [9]. The transmission mode in SEM was also shown to be promising for the investigation of nanoparticles [10].

Scanning electron microscopes can be equipped with numerous detectors for secondary electron (SE), backscattered electron (BSE) and STEM imaging due to less stringent space restrictions in the sample chamber. Taking STEM and SEM images simultaneously from the same specimen region will be referred to as correlative SEM/low-keV STEM in the following and is shown to provide complementary and comprehensive information from the same sample region [11]. For instance, a modern scanning electron microscope allows to simultaneously obtain topography contrast from SE-SEM images, material contrast from BSE-SEM images, Bragg diffraction contrast from bright-field (BF)-STEM images and mass-thickness contrast from high-angle annular dark-field (HAADF)-STEM images. Recently, the application of SEM has been further extended by commercially available on-axis charge-coupled device (CCD) cameras [12] which enables the detection of Kikuchi and diffraction patterns for crystal structure analysis. In combination with a double-tilt sample holder, specimens can be oriented into specific diffraction conditions yielding the capability for defect analysis, e.g. Burgers vector determination, which could be previously performed only in transmission electron microscopes [13]. However, despite these developments, there are still only few studies, which emphasize the opportunities of STEM-in-SEM and correlative SEM/low-keV STEM.

This was the motivation for this work where we demonstrate the versatility of imaging in modern scanning electron microscopes and the opportunities of correlative SEM/low-keV STEM. We show results from detailed analyses of two exemplary nanostructured materials, namely multi-walled carbon nanotubes and a catalytically active material (Pt nanoparticles on  $\text{Al}_2\text{O}_3$ ). In addition, we will present for the first time HAADF-STEM tomography for three-dimensional (3D) reconstruction from a

tomographic tilt series obtained in a scanning electron microscope. The  $180^\circ$  tilt capability of our sample holder was exploited to obtain reconstructions without missing wedge artifact.

## Materials and methods

### Sample materials and specimen preparation

Commercially available multi-walled carbon nanotubes (CNTs) (CNT powder produced by SIGMA-ALDRICH, St. Louis, USA) were chosen as an exemplary sample to show the benefits of correlative SEM/low-keV STEM. The CNTs were deposited on a holey carbon film supported by a conventional TEM copper grid (Supplier: TED PELLA, Product number: 01824). For this purpose, the CNT powder was dispersed on the TEM grid. The second type of material used in this work is a Pt/ $\text{Al}_2\text{O}_3$  catalyst sample. The material consists of Pt nanoparticles (NPs) on  $\text{Al}_2\text{O}_3$  carrier particles with several 100 nm size obtained by the fabrication method outlined by Casapu et al. [14]. The Pt/ $\text{Al}_2\text{O}_3$  powder and distilled water were mixed by a ratio of 1:1000 (by weight fraction) and deposited by ultrasonic evaporation on a commercial copper grid covered with an ultrathin carbon layer on lacey carbon film (Supplier: TED PELLA, Product number: 657–200-CU).

A special sample was prepared for 3D reconstruction of CNTs that allows full  $180^\circ$  tilting experiments. For this purpose, CNTs were attached to the tip of a tungsten (W) micromanipulator needle (Plano GmbH, Wetzlar, Germany, type J411) by dipping the needle into the CNT powder. CNT bundles and single CNT stick to the W needle by adhesion forces. As the length of CNTs in the SIGMA-ALDRICH powder was limited, CNT powder by TCI (Tokyo Chemical Industry Co., Ltd., Tokyo, Japan, type C2156) was employed. The W needle was attached to a 4Pin-Lift-Out-Grid (PELCO type 10GC04) by first shortening the needle and then gluing it to the lift-out grid using G1/G2 epoxy (Gatan Inc., CA, Pleasanton, USA) under light microscopy control. An overview light microscopy image of the prepared specimen is shown in Fig. 1.

## Experimental setup

SEM and low-keV STEM were performed in a combined SEM/focused-ion-beam (FIB) Helios G4 FX system (Thermo Fisher Scientific, Waltham, Massachusetts, USA). The instrument is equipped with a Schottky field-emission gun and a STEM-4 semiconductor detector, which is positioned 40 mm below the objective lens pole piece. Electron-transparent samples can be loaded into the instrument with a double-tilt sample holder controlled by a compustage. The TEM sample holder facilitates a large tilt angle range of  $> 180^\circ$ , which was exploited in this work to perform tomography. By changing the distance between the double-tilt sample holder and the objective lens pole piece, the collection angle range of STEM detector can be changed. Working distances employed in this study were between 1.8 and 4.5 mm. Collection angles used for detecting transmitted electrons were up to 7 mrad for BF-STEM and 64–275 mrad for HAADF-STEM. High-resolution BF-STEM images with a resolution of about 0.3 nm were obtained in the immersion mode where the sample is located in the magnetic field of the objective lens. SEs were collected by the through-the-lens detector (TLD). A solid-state BSE detector located in the electron column above the TLD detector was applied for BSE collection. A retractable CCD camera (Bruker OPTIMUS<sup>TM</sup>) is mounted below the TEM specimen for the acquisition of on-axis transmission electron diffraction (TED) patterns for crystal structure analysis. A Titan<sup>3</sup> 80–300 TEM (Thermo Fisher Scientific) operated at 300 keV was used to take electron diffraction patterns for comparison with TED patterns acquired with the Helios G4 FX SEM.

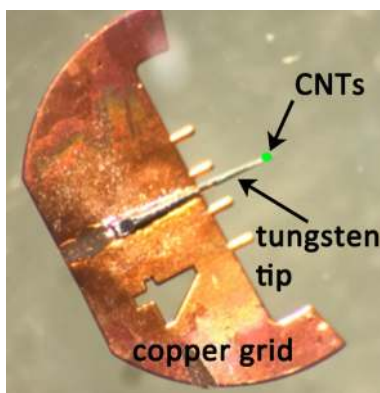


**Figure 1** Overview light microscopy image of the prepared CNT specimen for  $180^\circ$  tomography.

## Three-dimensional reconstruction by electron tomography

For HAADF-STEM tomography, projections of an electron transparent sample are recorded from multiple directions. This is commonly realized by rotating the sample around a single axis as schematically shown in Fig. 2a. Hereby, large tilt angles are mandatory to obtain meaningful 3D reconstructions. Up to now conventional STEM stages in scanning electron microscopes did not allow large tilt angles and, therefore, were not suited for 3D reconstruction by electron tomography. However, this limitation does not apply for the Helios G4 FX with a compustage and double-tilt sample holder. An image of the sample holder is shown in Fig. 2b. The STEM sample is mounted by a clip at the front of the rod (cf. magnified region in white frame in Fig. 2b) with the tilt axis  $\alpha$  and  $\beta$  indicated in the image. Both tilt axes provide a large tilt range of  $-10^\circ$  to  $170^\circ$  ( $\alpha$  axis) and  $-190^\circ$  to  $10^\circ$  ( $\beta$  axis). However, as  $\alpha$  tilting is performed by rotation of the sample rod, the overhead crossing blocks the transmitted beam at certain tilt angles. This does not apply for  $\beta$  tilt due to the absence of blocking structures (Fig. 2b) allowing to use the full tilt range in STEM mode.

Due to the lack of a suitable software, tilt series were acquired manually where at each step the feature of interest was centered and focused by the operator. The angle increment was  $5^\circ$  with an overall tilt angle range of up to  $180^\circ$  resulting in 36 sample projections.

Reconstructions were performed by the backprojection-based simultaneous iterative reconstruction technique (SIRT) algorithm [15, 16]. This algorithm requires mass-thickness contrast where the image intensity follows a monotonic function of the object's properties without contributions of Bragg-diffraction contrast. This requirement is fulfilled for incoherent HAADF-STEM imaging. The IMOD software (version 4.9.0) [17, 18] was used for 3D reconstruction. Segmentation is based on intensity thresholding. Segmentation and 3D rendering of the reconstructed structure was performed using the Avizo software package (FEI, version 9.3).

## Simulation of the HAADF-STEM intensity

HAADF-STEM is widely used for material contrast (Z contrast) imaging because the large collection



**Figure 2** **a** Simplified scheme of HAADF-STEM tomography. **b** Photograph of STEM sample holder of the Helios G4 FX. The front region of the rod (marked by a white rectangle) is magnified in the photograph below with  $\alpha$ -tilt and  $\beta$ -tilt directions indicated.

angles chosen for HAADF-STEM allow mainly the detection of incoherent elastic scattered electrons [19–21]. For quantitative understanding of HAADF-STEM images, comparison between experimental and simulated STEM intensity is required. This applies in particular for HAADF-STEM at low electron energies, where  $Z$  contrast from experimental HAADF-STEM images can be counterintuitive because materials with higher atomic number appear darker than materials with lower atomic number due to the thickness dependence of HAADF-STEM imaging [22]. One way to simulate STEM intensities is based on solving the analytical transport equation [23] with the scattering distribution of the multiple scattered electrons evaluated numerically by using a series of Legendre polynomials [24]. Within this work, we used the software CeTE 1.4 [11] to support understanding of the experimentally observed HAADF-STEM intensities. In the simulations, screened Rutherford differential cross-sections for elastic electron scattering were used.

## Results and discussion

By combining SEM and low-keV STEM in a correlative way, the inner and outer structure of CNTs can be imaged as demonstrated in Fig. 3. The 2 keV SE-SEM image in Fig. 3a displays topography information emphasizing the smooth surface and spatial arrangement of CNTs. A corresponding 30 keV BF-STEM image is shown in Fig. 3b where the dark features within the CNTs (e.g. feature marked by black arrow) are the result of changes of the diffraction conditions. Additionally, the hollow inner CNT structure becomes obvious. BF-STEM also indicates that the crystalline CNTs are covered by amorphous material most likely resulting from contamination. The low BF-STEM intensity marked by the white

arrow in Fig. 3b can be understood by the overlap of two CNTs observed in the SE-SEM image (white arrow in Fig. 3a) leading to a substantial increase of the local sample thickness. SE-SEM and BF-STEM images of a magnified region (black rectangle in Fig. 3b) were simultaneously recorded at 30 keV (cf. Figure 3c, d). This characterization procedure is especially advantageous for beam-sensitive materials since surface and inner structure are imaged simultaneously. The SE-SEM image reveals topography features on a scale in the order of 10 nm. State-of-the-art scanning electron microscopes are also capable of phase contrast imaging. The interference of diffracted and undiffracted beams on the BF-STEM detector reveals lattice fringes. To achieve the interference of diffracted and undiffracted beams, large electron-beam convergence angles are necessary [25]. These conditions are realized in the immersion mode where the sample is situated in the strong magnetic field of the objective lens. The inset in Fig. 3d reveals 3.3 Å lattice fringes in a high-resolution BF-STEM image, which matches the graphite interplanar distance of 3.36 Å [26]. In addition, the amorphous structure of the cover layer is clearly visible.

Two more CNT lattice-fringe images and the corresponding Fourier transformations (FTs) are shown in Fig. 4. The clear visibility of the fringes from a multi-walled CNT in Fig. 4a is emphasized by the (002) reflections indicated by white circles in the inset in Fig. 4(a). Lattice fringes are even observed in the overlap region of two CNTs shown in Fig. 4b, which are oriented almost perpendicular to each other. Despite the noise in Fig. 4b, the reflections are clearly visible in the FT (inset in Fig. 4b).

The advantage of combined SEM/low-keV STEM is further illustrated by Fig. 5 with the investigation of a second CNT sample. The large tilt range of the sample holder facilitates sample flipping and, hence, acquisition of SE topography images from both sides

**Figure 3** Combined SEM/low-keV STEM imaging of CNTs with **a** 2 keV SE-SEM overview image, **b** 30 keV BF-STEM overview image of the same region as **a**, simultaneously obtained high-magnification 30 keV **c** SE-SEM image and **d** BF-STEM image from the region marked by a black rectangle in **b**. The inset in **d** displays a magnified high-resolution BF-STEM image from the region marked by white square.

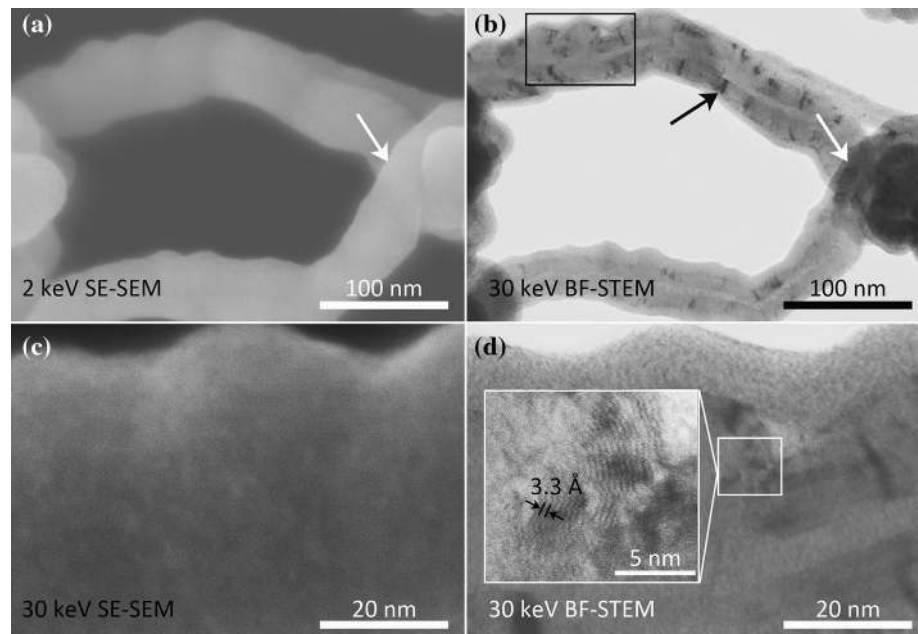


**Figure 4** 30 keV BF-STEM lattice-fringe images of **a** one multi-walled CNT and **b** an overlap region of two CNTs. The insets in **a**, **b** are Fourier transform analyses of the images in **a**, **b**.

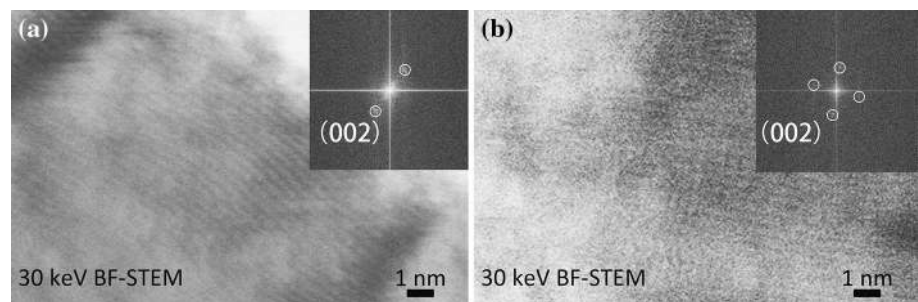
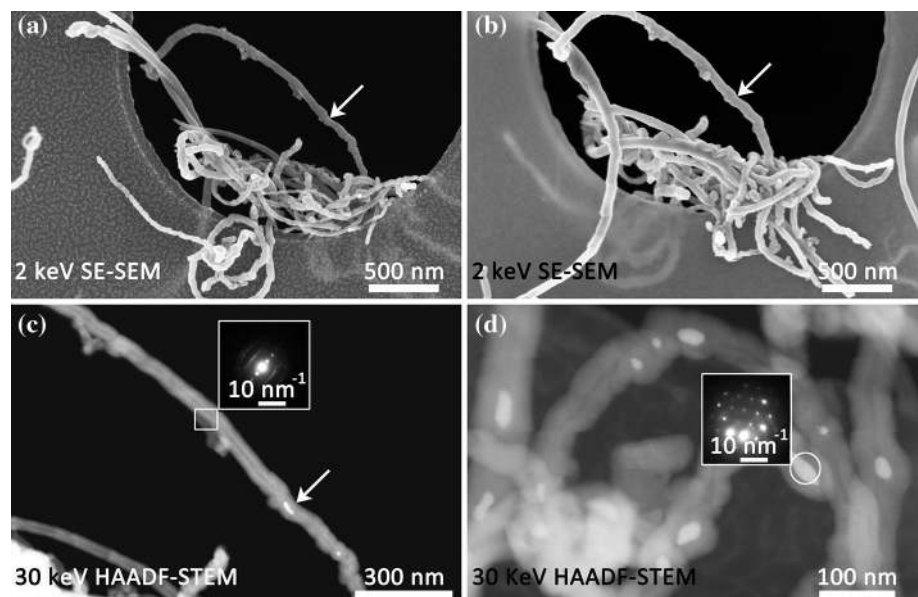


**Figure 5** Combined SEM/low-keV STEM imaging of CNTs. **a**, **b** 2 keV SE-SEM overview image from both sides of the sample, **c**, **d** magnified 30 keV HAADF-STEM images from regions in **a**, **b**. The inset in **c** shows a TED pattern from the square-marked region. The inset in **d** displays a TED pattern from the particle marked by a circle.



of the sample (Fig. 5a, b). HAADF-STEM imaging was carried out for two different regions in Fig. 5c, d. Regions with bright contrast in HAADF-STEM images demonstrate the presence of catalyst particles (one example indicated by a white arrow in Fig. 5c), which were used for CNT fabrication. In this case, the catalyst particles were a priori known to consist of Ni. The bright contrast can be rationalized by the higher atomic number of Ni ( $Z = 28$ ) compared to C ( $Z = 6$ ) resulting in a larger number of scattered electrons on the HAADF segment of the STEM detector. SE images of the same region (cf. arrows in Fig. 5a, b) did not show any surface feature related to the shape of the nanoparticle confirming that the Ni particle must be located within the CNT. The on-axis CCD-camera was employed to acquire TED patterns. The TED pattern shown in the inset in Fig. 5c was obtained by positioning the electron beam in the region marked by a small square. It displays reflections, which are expected for multi-walled CNTs with pronounced (001) reflections ( $l$  is an even number). Interestingly, the beam convergence angle of 2 mrad in the field-free mode is rather small giving rise to spot-like diffraction reflections. With a typical electron-beam diameter in the order of 1 nm and small convergence angles, TED in SEM facilitates nanodiffraction studies. A TED pattern obtained from the particle in Fig. 5d shows a pattern that is consistent with [101] zone-axis orientation of Ni.

Tomography is not only performed frequently in materials science but also in life sciences. Mass-thickness contrast in HAADF-STEM is well suited for tomography, which is extensively used in transmission electron microscopes [27]. HAADF-STEM tomography could not be performed in SEM up to now due to the limitation set by traditionally designed STEM stages and sample holders. With the implementation of a double-tilt holder and its capability of large tilt angle in the Helios G4 FX, low-keV HAADF-STEM tomography becomes feasible. Figure 6a, b shows 30 keV HAADF-STEM images of CNTs with tilt angles of  $0^\circ$  and  $-70^\circ$ , respectively. The images were extracted from a tilt series taken at eucentric height with an angular increment of  $5^\circ$  between images and a tilt-angle range of  $145^\circ$ .

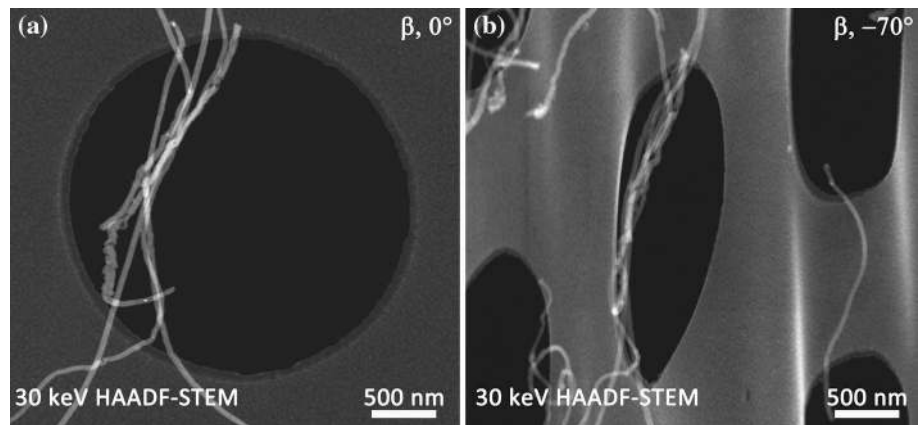
The 3D reconstruction of CNTs on a holey carbon film is shown in Fig. 7a. The surface topography of the carbon support film (grey color) and the spatial arrangement of the CNTs (green color) are clearly recognized in Fig. 7a. A magnified region of Fig. 7a is

presented in Fig. 7b, which shows CNTs and a NP embedded in a CNT (marked by red color and an arrow). A tilt angle increment of  $5^\circ$  was chosen due to time-consuming manual image acquisition as no automated tomography acquisition software is available for SEM instruments. Smaller angle increments can further improve resolution within the final 3D reconstruction. The tilt-angle range of this image series was limited to  $145^\circ$  not by the sample holder, but by the sample itself. The carbon support film and copper grid completely block the electron beam at large tilt angles. It is well known that reconstructions based on images series with limited tilt-angle range suffer from the so-called missing wedge artifact leading to elongation of sample features in electron propagation direction with decreasing tilt-angle range [28, 29].

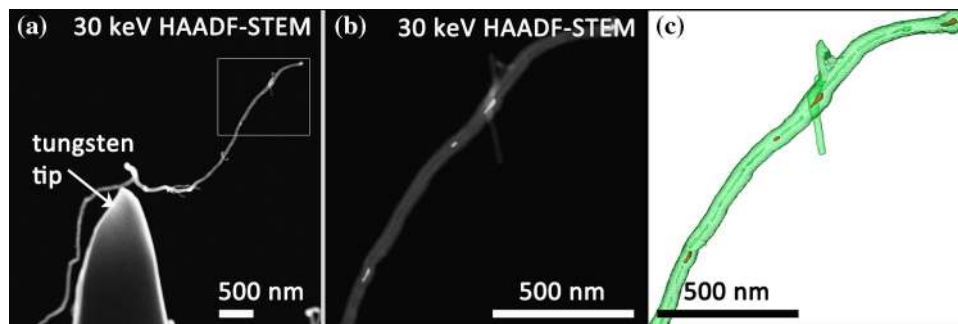
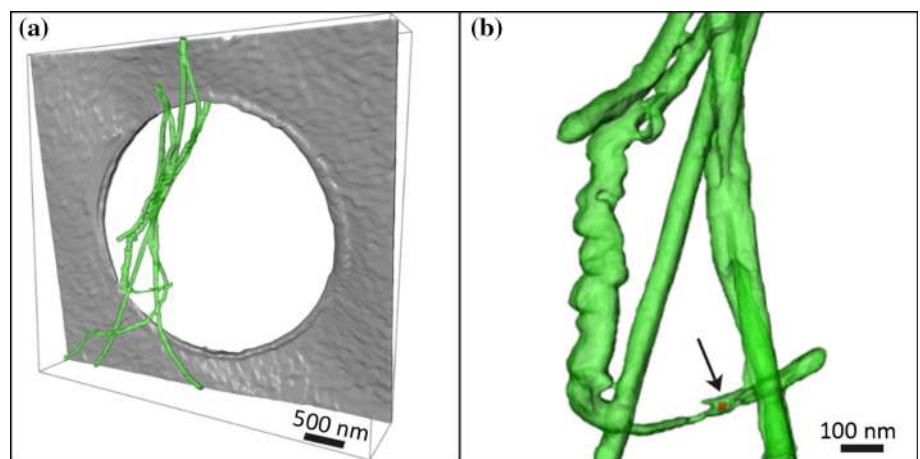
To overcome this problem, a second CNT sample was prepared as described in “Sample materials and specimen preparation” section. Figure 8a shows an overview HAADF-STEM image of the tip of the W needle with free-standing CNTs, which facilitates  $180^\circ$  sample tilt without blocking the electron beam. A low-keV HAADF-STEM tomography series with full  $180^\circ$   $\beta$ -tilt range and  $5^\circ$  angular increments was taken from the rectangle-marked area in Fig. 8a. Reconstruction was performed using the same tomography parameters as in Fig. 7. One of the HAADF-STEM images and the resulting rendered 3D reconstruction are shown in Fig. 8b, c. The arrangement of CNTs and Ni NPs are clearly visible in Fig. 8c. However, the full tilt range in Fig. 8 results in a stronger contrast in the reconstruction than in Fig. 7 allowing even the identification of the small-diameter hollow tube within the multi-walled CNT in Fig. 8c.

The second analyzed specimen is a Pt/ $\text{Al}_2\text{O}_3$  catalyst, which consists of  $\text{Al}_2\text{O}_3$  powder with particle sizes in a few 100 nm range and Pt NPs deposited on the  $\text{Al}_2\text{O}_3$ . This material can be used, e.g., for the oxidation of carbon monoxide [14]. The material morphology was studied by acquiring SE-SEM images. Different electron energies of 2, 5 and 30 keV (cf. Figure 9a–c) were tested to identify the electron energy where charging of  $\text{Al}_2\text{O}_3$  is minimized and topography contrast is optimized. The insets in Fig. 9a–c show magnified image sections. Figure 9b obtained at 5 keV best resolves small-scale  $\text{Al}_2\text{O}_3$  topography features in comparison with Fig. 9a, c. Using lower electron energies like 2 keV leads to enhanced charging. For higher electron energies like

**Figure 6** 30 keV HAADF-STEM images of CNTs acquired at  $\beta$ -tilt angles **a**  $0^\circ$  and **b**  $-70^\circ$ .



**Figure 7** Tomography images of CNTs reconstructed from 30 keV HAADF-STEM images: **a** an overview of CNTs on holey carbon film with  $\beta$  tilting range  $145^\circ$ , **b** a magnified image from one area in **a**.



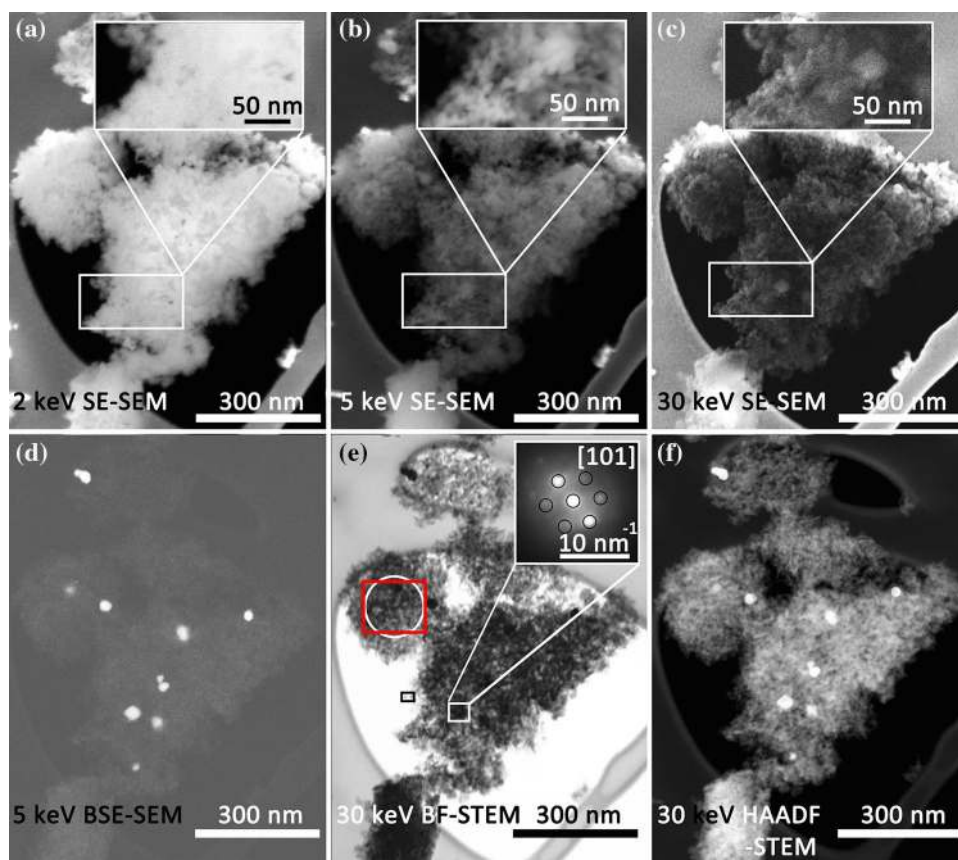
**Figure 8** **a** An overview 30 keV HAADF-STEM image of CNTs attached at the tungsten (W) tip. The area recorded for the  $180^\circ$  tilt series is marked by a white rectangle. **b** 30 keV HAADF-STEM

image of a CNT from a  $180^\circ$  tilt series, and **c** segmented 3D reconstruction showing CNTs, Ni catalyst particles (red) and the hollow tube within the CNT.

30 keV, the signal-to-noise ratio decreases due to the reduced secondary electron yield. Although SE detectors are implemented in some transmission electron microscopes, SE imaging in SEM is superior regarding topography contrast due to the substantially larger secondary electron yields at low electron energies. The BSE image Fig. 9d displays material contrast and allows to image larger Pt NPs with

remarkably high contrast with respect to  $\text{Al}_2\text{O}_3$ . The BF-STEM image Fig. 9e visualizes the porosity of the  $\text{Al}_2\text{O}_3$  particle. Pt NPs show darker contrast than the  $\text{Al}_2\text{O}_3$  due to dominant Bragg-diffraction contrast in BF-STEM. The TED pattern (inset in Fig. 9e) obtained from Pt particle marked by the white rectangular frame is consistent with Pt close to a [101] zone-axis. The contrast of Pt NPs and  $\text{Al}_2\text{O}_3$  is reversed in the

**Figure 9** SEM/low-keV STEM imaging of Pt/Al<sub>2</sub>O<sub>3</sub>: SE-SEM images of the same area taken with **a** 2 keV, **b** 5 keV, **c** 30 keV. **d** 5 keV BSE-STEM image of the same region as **a–c**. **e** 30 keV BF-STEM and **f** HAADF-STEM images obtained simultaneously with **c**. The insets in **a–c** display the magnified images from the corresponding rectangle-marked regions. The inset in **e** displays the TED pattern from the region marked by a white square.



30 keV HAADF-STEM image Fig. 9f with Pt NPs showing strong atomic-number contrast. We note that correlative SEM/low-keV STEM is particularly advantageous to study nanomaterials with a pronounced topography. This information is not available by (S) TEM alone but nevertheless strongly influences (S) TEM contrast.

TED patterns were taken for crystal structure analysis in the Helios G4 FX and for comparison in the Titan<sup>3</sup> 80–300. The region marked by a red rectangle in Fig. 9e was scanned in the Helios G4 FX while recording the TED pattern in Fig. 10a. By choosing a long exposure time for the CCD camera in the Helios G4 FX, the diffraction patterns are integrated over the whole region yielding a selected area electron diffraction (SAED)-like pattern. This is possible because the undiffracted beam on the camera does not move significantly while scanning over a moderate-sized sample region ( $\sim 10^4$  nm<sup>2</sup>). Due to the large number of different Al<sub>2</sub>O<sub>3</sub> crystal orientations within the scanned area, the diffraction pattern resembles a powder diffraction pattern. For comparison, the region marked by white circle in Fig. 9e was imaged in the Titan microscope with the SAED

aperture placed at the same sample region. The resulting SAED pattern is shown in Fig. 10b. We note that the regions, where the diffraction information was obtained, are not exactly identical due to the different geometry of the circular SAED aperture in TEM and the rectangular shape of the scanned region in SEM. However, both diffraction patterns (Fig. 10a, b) show reflection rings. The diffraction pattern quality in SEM is lower compared to the one in TEM, which is attributed to the poor modulation transfer function (MTF) of the employed CCD-camera and the limited ability to change the camera length. Both issues should be addressed in future diffraction studies in scanning electron microscopes. In addition, enhanced inelastic scattering of comparatively thick specimens adds background noise that degrades the quality of low-energy electron diffraction patterns. The intensity of the TED patterns was integrated azimuthally and is displayed as radial profile superimposed in Fig. 10a, b (white curves). The experimental curves agree well with simulated powder TED patterns (cf. green lines in Fig. 10a, b) for  $\gamma$ -Al<sub>2</sub>O<sub>3</sub> with cubic structure (Fd-3 m, lattice parameter 0.791 nm [30]). Hence, Fig. 10



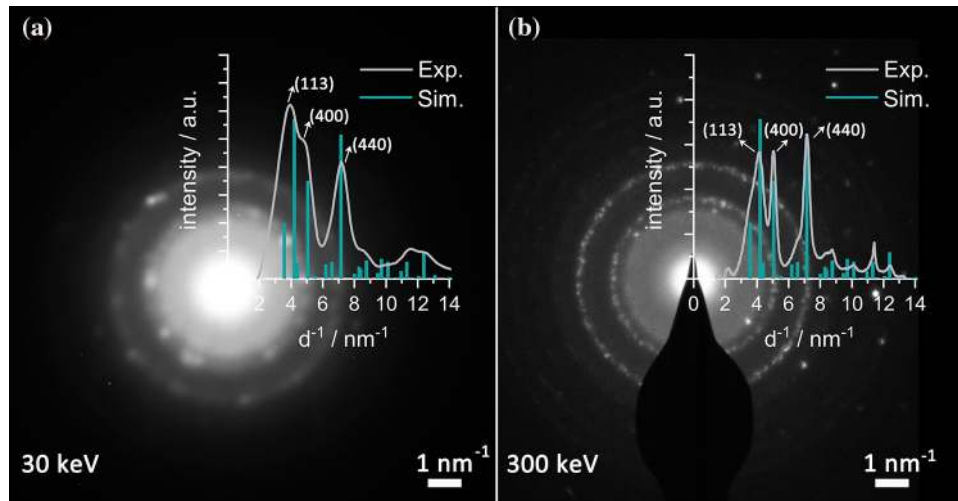


**Figure 10** TED patterns obtained **a** at 30 keV with the Helios G4 FX and **b** at 300 keV with the FEI Titan<sup>3</sup> 80–300. For the acquisition of the TED pattern in the Helios G4 FX, the region in the red rectangle in Fig. 9e was scanned. The region within the

demonstrates the possibility of using SEM for diffraction analyses of polycrystalline or even amorphous materials.

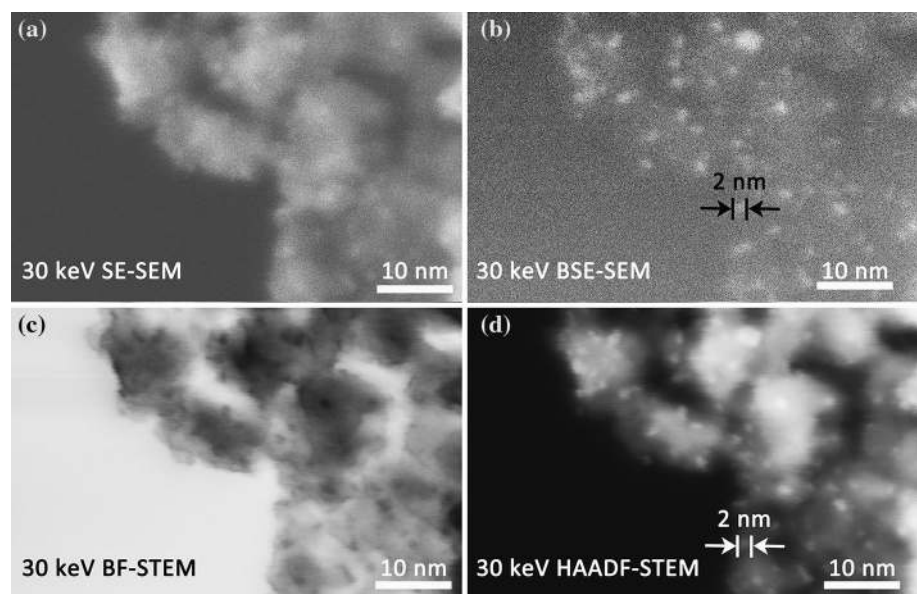
For the small region marked by a black rectangle in Fig. 9e, high-magnification 30 keV SE, BSE and STEM images were acquired simultaneously within one scan as shown in Fig. 11. The BSE (Fig. 11b) and HAADF (Fig. 11d) images show a large density of Pt NPs with a size of approximately 2 nm (cf. marks in Fig. 11b, d). Pt NPs are not obvious in the SE-SEM image Fig. 11a, which mainly visualizes Al<sub>2</sub>O<sub>3</sub>

circular white frame in Fig. 9e was selected for the SAED pattern acquired with the FEI Titan<sup>3</sup> 80–300. The azimuthally integrated intensity as a function of scattering angle and the simulated intensity for  $\gamma$ -Al<sub>2</sub>O<sub>3</sub> are superimposed in (a) and (b).

topography in this very thin specimen region. The change of the local Al<sub>2</sub>O<sub>3</sub> thickness results in corresponding changes of the Al<sub>2</sub>O<sub>3</sub> intensity in the BF-STEM and HAADF-STEM images. The BF-STEM image Fig. 11c also displays the Pt NPs but with reduced contrast compared to the HAADF-STEM and BSE-SEM images.

A phenomenon discovered from Pt/Al<sub>2</sub>O<sub>3</sub> is contrast inversion of Pt NPs and Al<sub>2</sub>O<sub>3</sub> in HAADF-STEM images (cf. Figure 12a, b). Depending on the Pt particle size and Al<sub>2</sub>O<sub>3</sub> thickness, Pt NPs can show either

**Figure 11** High-magnification correlative 30 keV SEM/low-keV STEM images of Pt/Al<sub>2</sub>O<sub>3</sub>. **a** SE-SEM, **b** BSE-SEM, **c** BF-STEM and **d** HAADF-STEM images of the same area obtained simultaneously.



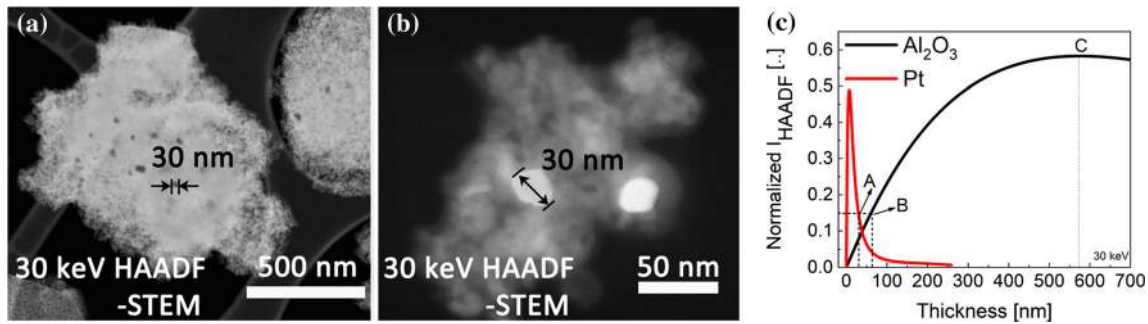


**Figure 12** a, b 30 keV HAADF-STEM imaging of Pt/Al<sub>2</sub>O<sub>3</sub> [31]. c 30 keV HAADF-STEM intensity simulations by CeTE 1.4 as a function of thickness for both Pt and Al<sub>2</sub>O<sub>3</sub> materials.

dark (cf. Figure 12a) or bright (cf. Figure 12b) contrast with respect to Al<sub>2</sub>O<sub>3</sub>. Simulations of the HAADF-STEM intensity (cf. Figure 12c) are used to understand this observation. The HAADF-STEM intensity, normalized with respect to the total number of simulated electrons, is shown as a function of sample thickness in Fig. 12c for Pt (red curve) and Al<sub>2</sub>O<sub>3</sub> (black curve). The HAADF-STEM intensity first rises with the sample thickness up to a maximum value. This is caused by the increasing number of electrons scattered into large angles, which are collected by the HAADF-STEM detector. With further increase in the thickness, however, the HAADF-STEM intensity decreases because electrons are scattered beyond the scattering angle range of the HAADF-STEM detector segment. For materials with high atomic number like Pt, the intensity maximum occurs at a small thickness compared to Al<sub>2</sub>O<sub>3</sub> where the maximum is only reached at 575 nm sample thickness (label C in Fig. 12c). For the following discussion, we assume the thickness of the Pt NPs to be similar as the lateral size (about 30 nm, cf. markers in Fig. 12a, b). According to the simulations in Fig. 12c, a Pt NP with 30 nm thickness has a normalized HAADF-STEM intensity of 0.15 (label A in Fig. 12c). The same normalized HAADF-STEM intensity corresponds to Al<sub>2</sub>O<sub>3</sub> with a thickness of 60 nm (label B in Fig. 12c). Hence, a 30 nm-thick Pt NP located on an Al<sub>2</sub>O<sub>3</sub> particle can be treated by adding roughly 60 nm of thickness to the thickness of the Al<sub>2</sub>O<sub>3</sub> particle. If the Al<sub>2</sub>O<sub>3</sub> substrate thickness is much smaller than the thickness where the HAADF-STEM intensity of Al<sub>2</sub>O<sub>3</sub> reaches its highest value (C in Fig. 12c at a thickness  $t_{\max} = 575$  nm), adding an extra of 60 nm would lead to an increase in normalized HAADF intensity and corresponding bright contrast of the Pt NP. A region with such a low Al<sub>2</sub>O<sub>3</sub>

thickness is seen in Fig. 12b where the Pt NP shows bright contrast. However, if the thickness of the Al<sub>2</sub>O<sub>3</sub> particle is close to  $t_{\max}$  or larger, an increase in thickness would yield a lower normalized HAADF-STEM intensity. This leads to a reduction of the HAADF-STEM intensity for regions containing Pt NPs as exemplified in Fig. 12a.

## Conclusions

In this work, we have demonstrated that correlative SEM/ low-keV STEM imaging in a modern scanning electron microscope provides not only surface but also comprehensive volume information from the same specimen region. Transmission electron diffraction patterns with a small beam convergence angle can be recorded on an on-axis CCD camera with information from a nanoscaled or larger predefined region. The option to rapidly change the electron energy allows to efficiently optimize imaging conditions, e.g., to reduce sample charging as demonstrated for Al<sub>2</sub>O<sub>3</sub> particles. In our instrument, even 180° STEM tomography can be performed with suitable sample preparation to avoid the missing wedge artifact.

Most suitable objects for correlative SEM/low-keV STEM are nanostructured materials (e.g. small particles) where the low electron energy is not a limitation with regard to the specimen thickness. Other interesting objects are weakly scattering materials or materials that are sensitive towards air exposure. In the latter case, focused-ion-beam sample preparation in a combined FIB-SEM instrument and imaging can be performed without exposure to air. Low electron energies are also advantageous for samples suffering from knock-on damage. Simultaneous acquisition of

SEM and STEM signals within one scan contributes to the reduction of the total electron dose on the specimen.

Phase contrast BF-STEM imaging with resolution in the order of 3 Å is not yet competitive with STEM resolution in transmission electron microscopes but sufficient to solve numerous materials questions. Further resolution improvement can be envisioned by the implementation of an aberration corrector.

## Acknowledgements

Open Access funding provided by Projekt DEAL. We would like to thank Dr. Maria Casapu and Prof. Dirk Grunwaldt (Institute for Chemical Technology and Polymer Chemistry, Karlsruhe Institute of Technology) for supplying the Pt/Al<sub>2</sub>O<sub>3</sub> sample. We also would like to acknowledge funding from the DFG (Deutsche Forschungsgemeinschaft).

## Author contributions

CS and DG conceived the experiments. CS, SL and MM performed the experiments. CS, DG and MM wrote the manuscript. EM significantly contributed to the discussion and interpretation.

## Compliance with ethical standards

**Conflict of interest** The authors declare that they have no conflict of interest.

**Electronic supplementary material:** The online version of this article (<https://doi.org/10.1007/s10853-020-04970-3>) contains supplementary material, which is available to authorized users.

**Open Access** This article is licensed under a Creative Commons Attribution 4.0 International License, which permits use, sharing, adaptation, distribution and reproduction in any medium or format, as long as you give appropriate credit to the original author(s) and the source, provide a link to the Creative Commons licence, and indicate if changes were made. The images or other third party material in this article are included in the article's Creative Commons licence, unless indicated otherwise in a credit line to the material. If material is not included in the article's Creative Commons licence and your intended use is

not permitted by statutory regulation or exceeds the permitted use, you will need to obtain permission directly from the copyright holder. To view a copy of this licence, visit <http://creativecommons.org/licenses/by/4.0/>.

## References

- [1] Cowley JM (1969) Image contrast in a transmission scanning electron microscope. *Appl Phys Lett* 15:58. <https://doi.org/10.1063/1.1652901>
- [2] Bogner A, Jouneau P-H, Thollet G, Basset D, Gauthier C (2007) A history of scanning electron microscopy developments: towards “wet-STEM” imaging. *Micron* 38:390–401. <https://doi.org/10.1016/j.micron.2006.06.008>
- [3] Van Ngo V, Hern M, Roth B, Joy DC (2007) STEM imaging of lattice fringes and beyond in a UHR in-lens field-emission SEM. *Microscopy Today* 15:12–16. <https://doi.org/10.1017/S1551929500050951>
- [4] Klein T, Buhr E, Georg Frase C (2012) TSEM: a review of scanning electron microscopy in transmission mode and its applications. *Adv Imag Elect Phys* 171:297–356
- [5] Bell DC, Mankin M, Day RW, Erdman N (2014) Successful application of low voltage electron microscopy to practical materials problems. *Ultramicroscopy* 145:56–65. <https://doi.org/10.1016/j.ultramic.2014.03.005>
- [6] Guise O, Strom C, Preschilla N (2011) STEM-in-SEM method for morphology analysis of polymer systems. *Polymer* 52:1278–1285. <https://doi.org/10.1016/j.polymer.2011.01.030>
- [7] Drummy LF, Yang J, Martin DC (2004) Low-voltage electron microscopy of polymer molecular thin films. *Ultramicroscopy* 99:247–256. <https://doi.org/10.1016/j.ultramic.2004.01.011>
- [8] Pfaff M, Klein MFG, Müller E, Müller P, Colsmann A, Lemmer U, Gerthsen D (2012) Nanomorphology of P3HT:PCBM-based absorber layers of organic solar cells after different processing conditions analyzed by low-energy scanning transmission electron microscopy. *Microsc Microanal* 18:1380–1388. <https://doi.org/10.1017/S143192761201344X>
- [9] Kuwajima M, Mendenhall JM, Lindsey LF, Harris KM (2013) Automated transmission-mode scanning electron microscopy (tSEM) for large volume analysis at nanoscale resolution. *PLoS ONE* 8:e59573. <https://doi.org/10.1371/journal.pone.0059573>
- [10] Buhr E, Senfleben N, Klein T, Bergmann D, Gnieser D, Frase CG, Bosse H (2009) Characterization of nanoparticles by scanning electron microscopy in transmission mode.

- Meas Sci Technol 20:084025. <https://doi.org/10.1088/0957-0233/20/8/084025>
- [11] Sun C, Müller E, Meffert M, Gerthsen D (2018) On the progress of scanning transmission electron microscopy (STEM) imaging in a scanning electron microscope. *Microsc Microanal* 24:99–106. <https://doi.org/10.1017/S1431927618000181>
- [12] Brodu E, Bouzy E, Fundenberger J-J, Guyon J, Guitton A, Zhang Y (2017) On-axis TKD for orientation mapping of nanocrystalline materials in SEM. *Mater Character* 130:92–96. <https://doi.org/10.1016/j.matchar.2017.05.036>
- [13] Sun C, Müller E, Meffert M, Gerthsen D (2019) Analysis of crystal defects by scanning transmission electron microscopy (STEM) in a modern scanning electron microscope. *Adv Struct Chem Imag* 5:1. <https://doi.org/10.1186/s40679-019-0065-1>
- [14] Casapu M, Fischer A, Gänzler AM, Popescu R, Crone M, Gerthsen D, Türk M, Grunwaldt J-D (2016) Origin of the normal and inverse hysteresis behavior during CO oxidation over Pt/Al<sub>2</sub>O<sub>3</sub>. *ACS Catal* 7:343–355. <https://doi.org/10.1021/acscatal.6b02709>
- [15] Leary RK, Midgley PA (2019) *Electron tomography in materials science*. Springer, Switzerland AG, p 1279
- [16] Gilbert P (1972) Iterative methods for the three-dimensional reconstruction of an object from projections. *J Theor Biol* 36:105–117. [https://doi.org/10.1016/0022-5193\(72\)90180-4](https://doi.org/10.1016/0022-5193(72)90180-4)
- [17] Kremer JR, Mastrorade DN, Mcintosh JR (1996) Computer visualization of three-dimensional image data using IMOD. *J Struct Biol* 116:71–76. <https://doi.org/10.1006/jsbi.1996.0013>
- [18] Mastrorade DN, Held SR (2017) Automated tilt series alignment and tomographic reconstruction in IMOD. *J Struct Biol* 197:102–113. <https://doi.org/10.1016/j.jsb.2016.07.011>
- [19] Howie A (1979) Image contrast and localized signal selection techniques. *J Microsc* 117:11–23. <https://doi.org/10.1111/j.1365-2818.1979.tb00228.x>
- [20] Hartel P, Rose H, Dinges C (1996) Conditions and reasons for incoherent imaging in STEM. *Ultramicroscopy* 63:93–114. [https://doi.org/10.1016/0304-3991\(96\)00020-4](https://doi.org/10.1016/0304-3991(96)00020-4)
- [21] Nellist PD, Pennycook SJ (1999) Incoherent imaging using dynamically scattered coherent electrons. *Ultramicroscopy* 78:111–124. [https://doi.org/10.1016/S0304-3991\(99\)00017-0](https://doi.org/10.1016/S0304-3991(99)00017-0)
- [22] Čalkovský M, Müller E, Hugenschmidt M, Gerthsen D (2019) Differential electron scattering cross-sections at low electron energies: the influence of screening parameter. *Ultramicroscopy* 207:112843. <https://doi.org/10.1016/j.ultramicro.2019.112843>
- [23] Goudsmit S, Saunderson JL (1940) Multiple scattering of electrons. *Phys Rev* 57:24–29. <https://doi.org/10.1103/PhysRev.57.24>
- [24] Bethe HA, Rose ME, Smith LP (1938) The multiple scattering of electrons. *P Am Philos Soc* 78:573–585. <https://www.jstor.org/stable/984803>
- [25] Konno M, Ogashiwa T, Sunaoshi T, Orai Y, Sato M (2014) Lattice imaging at an accelerating voltage of 30 Kv using an in-lens type cold field-emission scanning electron microscope. *Ultramicroscopy* 145:28–35. <https://doi.org/10.1016/j.ultramicro.2013.09.001>
- [26] Belin T, Epron F (2005) Characterization methods of carbon nanotubes: a review. *Mater Sci Eng B* 119:105–118. <https://doi.org/10.1016/j.mseb.2005.02.046>
- [27] Li M, Yang Y, Huang B, Luo X, Zhang W, Han M, Ru J (2014) Development of advanced electron tomography in materials science based on TEM and STEM. *Trans Nonferrous Met Soc China* 24:3031–3050. [https://doi.org/10.1016/S1003-6326\(14\)63441-5](https://doi.org/10.1016/S1003-6326(14)63441-5)
- [28] Ke X, Bals S, Cott D, Hantschel T, Bender H, Van Tendeloo G (2010) Three-dimensional analysis of carbon nanotube networks in interconnects by electron tomography without missing wedge artifacts. *Microsc Microanal* 16:210–217. <https://doi.org/10.1017/S1431927609991371>
- [29] Wang XY, Lockwood R, Malac M, Furukawa H, Meldrum A (2012) Reconstruction and visualization of nanoparticle composites by transmission electron tomography. *Ultramicroscopy* 113:96–105. <https://doi.org/10.1016/j.ultramicro.2011.11.001>
- [30] Li FH, Cheng YF (1990) A simple approach to quasicrystal structure and phasen defect formulation. *Acta Cryst* A46:142–149. <https://doi.org/10.1107/S0108767389011323>
- [31] Sun C, Müller E, Gerthsen D (2019) On the benefits of obtaining surface topography and volume structure information by correlative S(T)EM in a scanning electron microscope. *Microsc Microanal* 25(S1):73–74. <https://doi.org/10.1017/S1431927618016094>

**Publisher's Note** Springer Nature remains neutral with regard to jurisdictional claims in published maps and institutional affiliations.